HiSST: 3rd International Conference on
High-Speed Vehicle Science Technology
14 -19 April 2024, Busan, Korea

Relative Navigation Implementation for the In-Air Capturing of a Winged Reusable Launch Vehicle

Sunayna Singh[1], Briek Luyten[1], Marco Sagliano[1]

Abstract

In the 'In-Air Capturing' recovery mode, a winged rocket stage is captured mid-air by an aircraft and towed back to the launch site. A critical aspect of 'In-Air Capturing' involves a capturing device released from the towing aircraft, tasked with autonomously navigating to the launcher stage and connecting the vehicles with a tether. This operation demands high-precision close-range navigation sensors for the final docking maneuver. Hence, this paper proposes and studies different navigation solutions for the full-scale 'In-Air Capturing' application. A Vision-Based Navigation System (VisNav) is compared against the classical GPS/INS and a combined GPS/INS/VisNav navigation system. Simulations show that the GPS/INS/VisNav has a higher accuracy and provides a more robust navigation solution against model uncertainties and external disturbances.

Keywords: *In-Air Capturing, Reusable Launch Vehicles, Relative Navigation, VisNav, Capturing Device*

Nomenclature

Abbreviations

6DOF	Six degrees of freedom
ACCD	Aerodynamically Controlled Capturing Device
AoA	Angle of attack
CCD	Charge-coupled device
LOS	Line-of-sight
DSP	Digital Signal Processor
EKF	Extended Kalman filter
FoV	Field of view
GLSDC	Gaussian Least Squares Differential Correction
GPS	Global Positioning System
LiDAR	Light Detection and Ranging
INS	Inertial Navigation System
L/D	Lift-to-drag
MECO	Main engine cut-off
PSD	Position Sensing Diode
RLV	Reusable launch vehicle
SWaP	Size, Weight and Power
TA	Towing aircraft
VisNav	Vision-Based Navigation System

Symbols

$\boldsymbol{b_i}$ – Unit line of sight vector of beacon i in object space

$\boldsymbol{B_i}$ – Position vector of beacon i in object space

c – Beacon Visibility Condition

$\boldsymbol{C}$ – Transformation matrix between object space and image space

d – Beacon Mounting Diameter

D – Docking Cone Outer Diameter

D' – Docking Cone Inner Diameter

$\boldsymbol{f}(\theta, h)$ – Docking Cone Surface

FoE – Beacon Field of Emission Half Angle

FoV – Sensor Field of View Half Angle

L – ACCD Length

n – Number of Beacons

$\boldsymbol{n}$ – Pointing Vector

$\boldsymbol{o}$ – Position of the sensor in object space

$\mathbf{p}$ – Modified Rodrigues parameter indicating attitude of the sensor in object space

$\boldsymbol{p}$ – Line of Sight Vector in ACCD Body Frame

$\boldsymbol{P}$ – Position in ACCD Body Frame

R – Beacon Range

V – Beacon Visibility

y_i – Measured coordinates in horizontal direction in the image frame

z_i – Measured coordinates in vertical direction in the image frame

---

[1] *DLR Institute of Space Systems, Robert Hooke Straße, 1, 28359, Bremen, Germany*

α – RLV Relative Pitch Angle
γ – Docking Cone Half Angle
μ – Sensor Mounting Angle

Φ – Principle rotation angle for modified rodrigues parameter

1. Introduction

The 'In-Air Capturing' return mode is an innovative launcher recovery method that has shown great potential for cost reduction compared to the currently operational Reusable Launch Vehicles (RLVs). This approach, first proposed by DLR [1], involves capture of a winged rocket stage mid-air using an aircraft, which tows it back to the launch site. This eliminates the need for a supplementary propulsion system for landing and brings down the inert mass [2]. This further reduces the overall cost of recovery when compared to vertical landing recovery methods, which require significant amount of fuel during descent. An assessment of the performance of various RLV approaches and the associated cost-benefit of 'In-Air Capturing' is presented in [3] and [4], respectively.

The complete (generic) mission cycle of 'In-Air Capturing' is shown in Fig. 1. The mission starts with a vertical launch from the launch pad. At main engine cut off (MECO), the winged first stage separates from the launch vehicle and the second stage moves on to the orbit. The first stage then begins a ballistic re-entry such that its velocity is reduced from supersonic to subsonic through atmospheric braking. In the meantime, a towing aircraft (TA) loiters at approximately 10 km altitude until the RLV is in the vicinity. Then, between an altitude of 2 km and 8 km, the TA approaches the RLV to form a gliding parallel formation. During this maneuver, a capturing device is released from the TA, which autonomously connects the two bodies via a tether. Finally, the RLV is towed back to an airstrip, where it is released to land horizontally.

Since an essential aspect of 'In-Air Capturing' involves close proximity formation flying and eventual docking/ mating with the capturing device, a reliable and accurate relative navigation system is necessary. The system should operate effectively even in turbulent weather conditions and poor visibility situations. Redundancy in sensor systems is crucial to ensure a safe and successful flight, mitigating the impact of sensor failures. Data from multiple sensors can be fused to achieve higher accuracy and improve robustness. Lightweight sensors with high update rates and low processing requirements add to the efficacy of the system. Thus, these factors must be considered for the selection of sensors. This study will analyze potential close-range relative navigation solutions for the full-scale 'In-Air Capturing' application. The main focus will be on the capture system, which requires interaction between the capturing device and the RLV for precise maneuvering and mating.

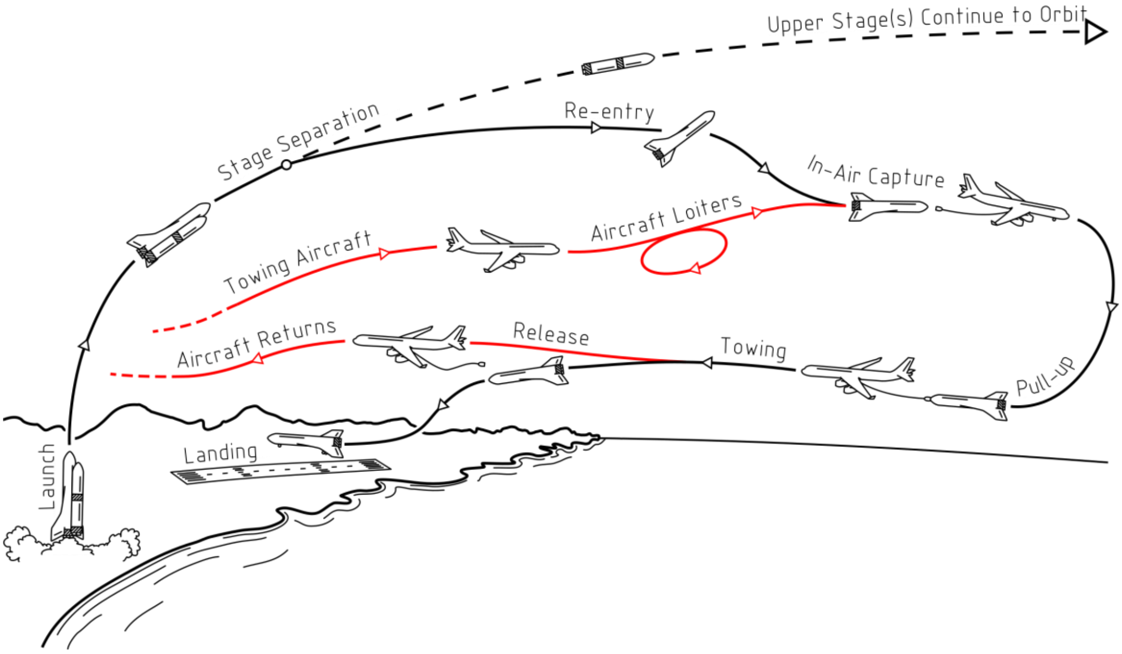

Fig. 1: Schematic of a typical In-Air Capturing mission cycle [1]

Similar scenarios to In-Air Capturing, which require precise close-range state estimation for rendezvous and docking can be found both in atmospheric flight and in space applications. In particular, the field of automated aerial refueling shows significant resemblance with the current application, and can offer a number of potential solutions to this relative navigation problem. A common approach is to use classical long-range sensors like the Global Positioning System (GPS) to calibrate the relative measurements from the relative Inertial Navigation Systems (INS) [6, 7]. This requires each aircraft or UAV to have the full GPS and INS sensor system. However, when precise measurements are required, GPS and INS based systems are often fused with other sensors (like electromagnetic detection systems), which can provide close-range, high-accuracy relative measurements [8, 9].

A prominent subset of these close-range sensors falls under the umbrella of computer vision. Computer vision systems typically use a generic, visible-wavelength camera, and rely on extensive image processing technologies to extract relevant data, such as relative position and attitude of a given target object. The cameras used can be grayscale [10] or color-sensitive [11], and can be mounted individually [12] or in pairs [13]. In some applications, the target body is left entirely unaltered and passive, purely relying on image processing algorithms, such as corner detection [14] and arc extraction [15]. Other systems depend on active markers that are applied to the target, and which increase the system's robustness to external lighting conditions [16]. One specific application, designed for boom-and-receptacle aerial refueling, employs a visual pressure snake sensor to detect a geometric pattern that has been applied to the target body [17].

Although computer vision techniques tend to achieve good performance with rates up to 55 Hz [18], and accuracies up to 10 cm [19], they come at the cost of significant computational power, which typically needs to be enabled using dedicated graphical processing units [20]. Additionally, the inherent reliance on visible-wavelength data creates a crucial sensitivity to environmental parameters, with most systems not being robust in low-light or low-visibility conditions [18]. One solution to this problem consists of shifting the relevant wavelength spectrum upwards, and using an infrared camera [21]. However, these solutions still require significant post-processing efforts.

Another major branch in this technological field can be found under electro-optical grid reference systems. A number of actively emitting beacons are mounted on the target, which a sensor on the main body detects. For the beacons, LEDs or laser diodes are typically used, while the sensor can be a Charge-Coupled Device (CCD detector), photodiode, or Position Sensing Diode (PSD) [22, 23]. Specific implementations of these systems include the VisNav technology developed at the Texas A&M University [24]. Contrary to computer vision techniques, these electro-optical grid reference systems are typically quite minimalistic in terms of Size, Weight and Power (SWaP) footprint, by relying on more elementary sensor elements which require less post-processing [23]. Additionally, when working with an IR-spectrum, the aforementioned robustness against environmental and lighting conditions can also be introduced [26].

Other solutions include ultrasonic or acoustic sensors [27], time-of-flight sensors [28], or radar technologies [22]. However, none of these are particularly suited to meet the In-Air Capturing requirements, respectively because of insufficient range and environmental robustness [29], and excessive power and size footprints [18]. Finally, LiDAR systems have also been used for these types of applications, either by using a scanning LiDAR [30], or a TriDAR system [31]. Although these systems are more robust to the effects of clouds, ambient light, and motion-blur [25], they suffer from attenuation due to atmospheric water vapour [22], while also having a significant SWaP footprint, with a relatively limited field of view (FoV) [33].

In conclusion, given the requirements of In-Air Capturing in terms of environmental robustness, accuracy, and SWaP, an electro-optical grid reference system for close-range navigation shows the greatest potential. In particular, VisNav technology is chosen as a potential solution for this application, and investigated in further detail. In Section 2, the theory and modelling of the VisNav system is reviewed. Additional models to simulate the VisNav system for In-Air Capturing applications are also presented in this section. This involves modelling of critical aspects like the line-of-sight (LOS) between RLV and ACCD, and placement of beacons on the ACCD to improve the likelihood of detection. Next, in Section 3, different sensor fusion configurations are proposed and analyzed. For performance analysis, VisNav is compared against a classic GPS/INS system and also, an integrated GPS/INS/VisNav system. It is assumed that the ACCD sends GPS and INS data to the RLV, where the sensor fusion process takes place. Simulations are then performed for both ideal and non-ideals scenarios using a simplified representation of 'In-Air Capturing' trajectory in Section 4. Finally, the conclusion and future work are discussed in Section 5.

2. Vision Based Relative Navigation System

The VisNav navigation system provides a six degrees of freedom (6DOF) solution constituting the relative position and orientation between two vehicles or objects at close-range (up to 200 m at 100 Hz [35]). It operates by evaluating the LOS vectors between a sensor, mounted on one vehicle, and a series of structured light beacons rigidly fixed to the target vehicle. These beacons have predetermined positions in the target vehicle frame, enabling the determination of the sensor's relative position and orientation with respect to the target frame [34]. A widely studied application for VisNav navigation systems is the probe-drogue aerial refueling system [23-24, 34-36].

The probe-drogue aerial refueling system consists of drogue attached to a hose released from the tanker aircraft as shown in Fig. 2. The back of the drogue has a conical skirt-like structure within which the VisNav beacons are typically placed. The receiver aircraft then navigates its way to the drogue and connects itself using a boom. The working principle being similar to the 'In-Air Capturing' application, supports the selection of VisNav for the relative navigation solution. Fig. 3 illustrates the configuration of the chosen capturing device for 'In-Air Capturing,' referred to as the Aerodynamically Controlled Capturing Device (ACCD). It measures 2 meters in length with a cross-sectional diameter of 1.5 meters, including the fins. Equipped with four flaps capable of deflecting up to a maximum of ±15°, it provides 6DOF for agility and control. The ACCD's nose is tethered to the TA via a rope, while the capturing mechanism located at the device's rear ensures a secure connection using a lock-in mechanism with a boom on the RLV. It also contains a guiding cone at the back, which could house the beacons for VisNav. The working principle and solution approach of Visnav is explained in Section 2.1.

Aerial refueling operations are typically performed at near constant altitude and velocity of the tanker aircraft. The receiver aircraft are usually highly maneuverable and can actively perform corrective maneuvers to reach the drogue. Conversely, the capture of the RLV during 'In-Air Capturing' is to be attempted in a descending formation flight as explained in [2]. The RLV, due to its lower aerodynamic performance, descends at a constant relative flight path angle of approximately -2° to the TA, even during the formation flight. Such a trajectory could lead to challenges in detection of the ACCD from the RLV and effective use of the VisNav technology. Thus, in Section 2.2, an analytical detection model is developed to analyze different configurations of beacons and placement of the VisNav sensor to improve the chances of successful detection. Finally, in Section 2.3, a sensitivity study is performed using this model, and the final configuration of VisNav for 'In-Air Capturing' application is selected.

Fig. 2: Aerial refuelling drogue with VisNav beacons and boom from the receiver aircraft [36]

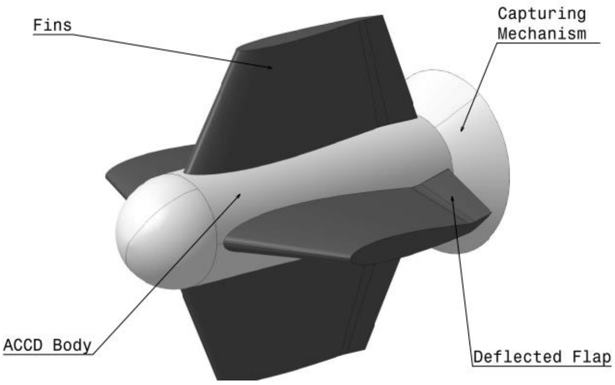

Fig. 3: Aerodynamically Controlled Capturing Device (ACCD) [37]

2.1. VisNav System

Fig. 4 shows a schematic of a VisNav sensor, when applied to the 'In-Air Capturing' application. The beacons, which can be actively controlled, are mounted on the cone located at the rear of ACCD (refer to Fig. 3). The sensor is mounted on the RLV body and comprises a Position Sensing Diode (PSD), wide-angle lens and a Digital Signal Processor (DSP). The beacons on the ACCD can be controlled to maintain different light intensities and activation sequences to ensure both preservation of the photo diode and optimal signal-to-noise ratio during operation [34]. During VisNav operation, as each beacon illuminates, light passes through the wide-angle lens, focusing onto the PSD. This focused light generates a centroid, or spot, on the photo diode, inducing a current imbalance across the four terminals on each side of the PSD. By measuring the voltage at each terminal, unit LOS vectors from the sensor to each beacon can be derived via a calibration function. Further details on the measurements and calibration with hardware can be found in [23].

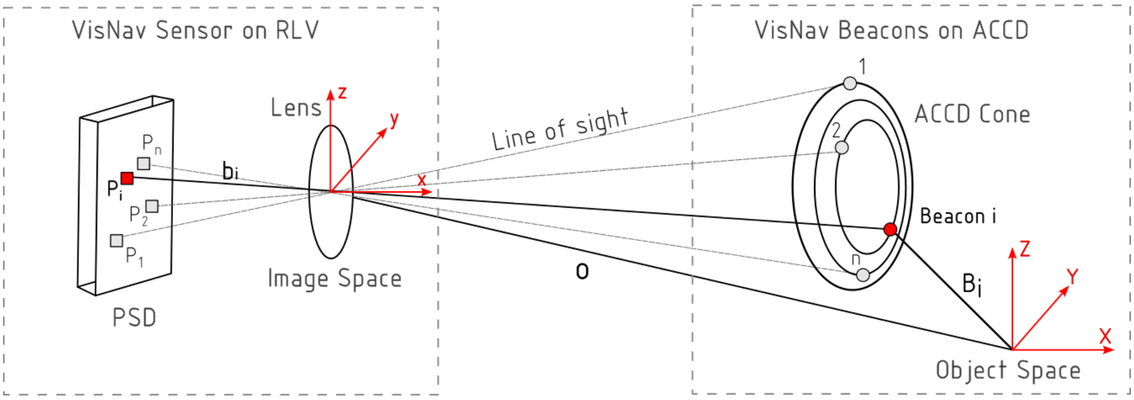

Fig. 4: VisNav sensor model applied to In-Air Capturing

Fig. 4 depicts two important coordinate frames. First, the object space frame is fixed to the ACCD body frame. The position of beacon i on the target vehicle is already known and its position vector in object space is denoted by $\boldsymbol{B_i}$. This can be written as:

$$\boldsymbol{B_i} = [\,X_i \quad Y_i \quad Z_i]^T \tag{1}$$

Second, the image space is a body-fixed frame located at the center of the lens on the sensor. The unit LOS vector of beacon i is measured from the image space to the PSD and is denoted by $\boldsymbol{b_i}$. Using this information, the position of the sensor in object space ($\mathbf{o}$), and the transformation matrix between image space and object space ($\boldsymbol{C}$) can be determined. They can be expressed using:

$$\mathbf{o} = [\,X_C \quad Y_C \quad Z_C]^T \tag{2}$$

And,

$$\boldsymbol{C} \;=\; \boldsymbol{I} \;+\; \frac{8\,[\mathbf{p}\;\times]^2 \;-\; 4\,(1-\mathbf{p}^{\boldsymbol{T}}\mathbf{p})[\mathbf{p}\times]}{(1-\mathbf{p}^{\boldsymbol{T}}\mathbf{p})^2} \tag{3}$$

Where,

$$[\mathbf{p}\times] = \begin{bmatrix} 0 & -\mathrm{p}_3 & \mathrm{p}_2 \\ \mathrm{p}_3 & 0 & -\mathrm{p}_1 \\ -\mathrm{p}_2 & \mathrm{p}_1 & 0 \end{bmatrix}$$

Here, the attitude parameterization is done using Modified Rodrigues Parameters (MRPs). They are a set of three attitude angles that can be linked to Euler parameters using principal rotation vector, $\boldsymbol{e}$, and principal rotation angle, Φ. Thus, the MRP (3x1) vector can be defined as $\mathbf{p} = \tan\frac{\boldsymbol{\Phi}}{4}\boldsymbol{e}$. Further explanation on the attitude parameters can be found in [38]. Using collinearity equations (described in detail in [36]), a nonlinear relationship between the measured image space coordinates (y_i, z_i), and the six unknown states in object space $(X_C,\ Y_C, Z_C,\ \mathrm{p}_1,\ \mathrm{p}_2,\ \mathrm{p}_3)$ can be established as follows:

$$y_i = -f\frac{C_{21}(X_i - X_c) + C_{22}(Y_i - Y_c) + C_{23}(Z_i - Z_c)}{C_{11}(X_i - X_c) + C_{12}(Y_i - Y_c) + C_{13}(Z_i - Z_c)} \tag{4}$$

$$z_i = -f\frac{C_{31}(X_i - X_c) + C_{32}(Y_i - Y_c) + C_{33}(Z_i - Z_c)}{C_{11}(X_i - X_c) + C_{12}(Y_i - Y_c) + C_{13}(Z_i - Z_c)} \tag{5}$$

Where f denotes the focal length of the wide-angle lens. Each beacon provides two equations through its measurements, necessitating a minimum of three beacons to derive a solution. However, to ensure a unique solution, a minimum of four measurements is required. A Gaussian Least Squares Differential Correction Algorithm (GLSDC) is used to solve for the position and orientation of the sensor with respect to the beacons. By integrating the measurement model and observation data, the algorithm generates an estimation of the unknown parameters that is optimal, considering a predetermined level of measurement noise [39]. A detailed explanation of the algorithm and the associated VisNav measurement model is given in [36].

2.2. Detection Model

In order to determine the visibility of each VisNav beacon, in conjunction with the relative states of both ACCD and RLV, a detection model is added to the simulation. The visibility of each beacon is calculated based on the geometry of the vehicles, the placement of each beacon on the ACCD and the placement of sensor on the RLV. The general configuration is shown in Fig. 5, which shows the relevant reference system and variables.

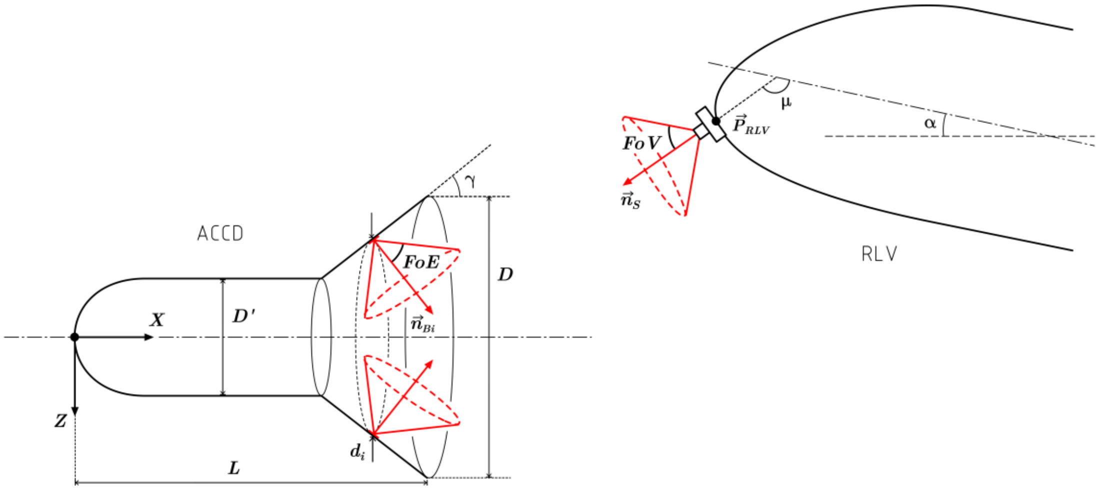

Fig. 5: Definition of reference system used in detection model

The detection model is based on a mathematical representation of the positions and normal vectors of all beacons and sensors. As a baseline configuration, a single sensor is mounted on the RLV. The RLV is modelled as a point mass with pitch angle α. The sensor position is assumed to be equal to the position of the RLV, $\boldsymbol{P}_{RLV}$. This position is derived from the trajectory model and is updated at the given sensor frequency (100 Hz). Since both RLV and ACCD are expected to have a positive pitch angle during the approach and capture, the sensor is mounted at an angle μ relative to the RLV orientation to increase visibility (see Fig. 5). Assuming only pitch variations in RLV, the corresponding sensor pointing vector $\boldsymbol{n}_S$ is given by:

$$\boldsymbol{n}_S = \begin{bmatrix} \cos(\alpha + \mu) \\ 0 \\ \sin(\alpha + \mu) \end{bmatrix} \tag{6}$$

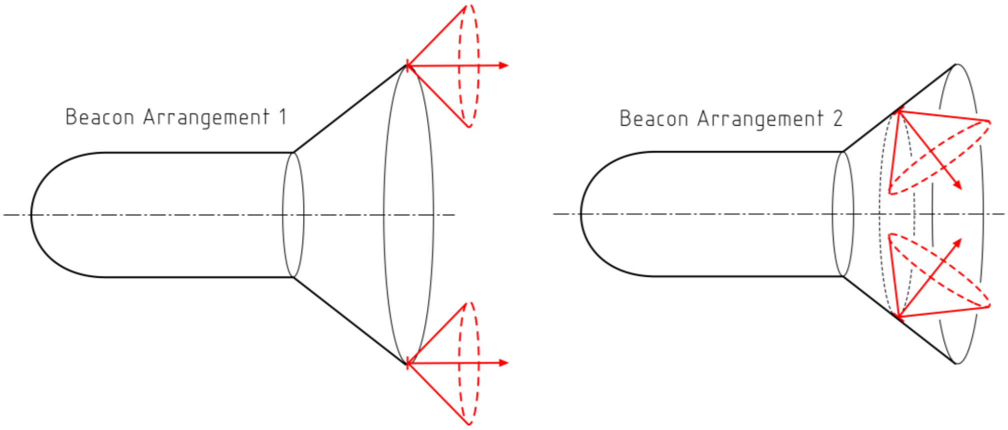

Fig. 6: Different types of beacon arrangements considered in the study

To improve the chances of detection, the beacons are mounted in two concentric arrangements on the ACCD cone. The first set of beacons are attached to the aft rim of the ACCD pointing along the positive X-axis of its body frame, seen in Fig. 6 as the outermost ring of beacons (Arrangement 1). This arrangement would facilitate detection from larger distances. Distributing n beacons equally over a circle with diameter d_i, results in the following position coordinates:

$$\boldsymbol{P_{Bi}} = \begin{bmatrix} L \\ d_i/2 \cdot \sin\phi_i \\ d_i/2 \cdot \cos\phi_i \end{bmatrix}, \quad \text{where} \quad \phi_i = i \cdot \frac{2\pi}{n}, \quad i = 1 \dots n \tag{7}$$

The second set of beacons are mounted inside the ACCD's docking cone, pointing slightly inwards (Arrangement 2 in Fig. 6). Such a configuration would facilitate precision mating at shorter distances. This docking cone is characterized by an outer diameter D, inner diameter D' and cone half angle γ, which allows it to be parametrized mathematically as a function of h and θ,

$$\boldsymbol{f}(h,\theta) = \begin{bmatrix} h \cdot \cos\gamma + L - D/(2 \cdot \tan\gamma) \\ h \cdot \sin\gamma \cdot \sin\theta \\ h \cdot \sin\gamma \cdot \cos\theta \end{bmatrix}, \quad \text{where} \quad \begin{cases} h \in [D'/(2 \cdot \sin\gamma),\ D/(2 \cdot \sin\gamma)] \\ \theta \in [0, 2\pi] \end{cases} \tag{8}$$

For a mounting circle of diameter d_i and mounting angle ϕ_i, $h = d_i/(2 \cdot \sin\gamma)$ and $\theta = \phi_i$. The pointing vectors $\boldsymbol{n_{Bi}}$ are equal to the unit normal vector to this surface, given by:

$$\boldsymbol{n_{Bi}}(h,\theta) = \left(\frac{\partial f}{\partial h} \times \frac{\partial f}{\partial \theta}\right) / \left\| \frac{\partial f}{\partial h} \times \frac{\partial f}{\partial \theta} \right\| \tag{9}$$

For a beacon to be successfully detected by the sensor, at least three conditions need to be fulfilled. The first one, c_{1i}, demands that the beacon be within the field of view of the sensor – defined as a half angle FoV. The sensor should also be within the beacon's field of emission (FoE_i), so that its emitted signal reaches the sensor. For this, an equivalent half angle FoE_i is defined for each beacon. In order to verify this condition, the LOS vector between each beacon and sensor is computed, and then compared to the pointing vectors of the corresponding beacon and sensor.

$$\boldsymbol{p_{BiS}} = (\boldsymbol{P_S} - \boldsymbol{P_{Bi}}) \,/\, \|\boldsymbol{P_S} - \boldsymbol{P_{Bi}}\| \tag{10}$$

As a second condition c_{2i}, the LOS vector should not be obstructed by any physical obstacle. In practice, the ACCD docking cone is the only potential source of obstruction in these configurations. The intersection point(s) between the LOS vector and cone surface are computed using Eq. (11) for unknown parameters h, θ, and t. Condition c_{2i} can then be checked by assuring that this intersection point lies outside of the physical ACCD cone – which can be done using the h-parameter of this point.

$$\boldsymbol{f}(h,\theta) = \boldsymbol{P_{Bi}} + \boldsymbol{p_{BiS}} \cdot t \quad \text{where} \quad \begin{cases} h \geq 0 \\ \theta \in [0, 2\pi] \\ t \geq 0 \end{cases} \tag{11}$$

Finally, as a third condition c_{3i}, the sensor should be within the beacon's range of emissivity R, so that its signal is strong enough to be detected. For this, the distance $\|\boldsymbol{P_S} - \boldsymbol{P_{Bi}}\|$ between sensor and beacon is used. Combining these three conditions, the overall visibility of each beacon can be assessed as follows:

$$V_i \Leftrightarrow (c_{1i} \wedge c_{2i} \wedge c_{3i}) \quad \text{where} \begin{cases} c_{1i} = \left(\cos^{-1}(\boldsymbol{p_{BiS}} \cdot \boldsymbol{n_{Bi}}) \leq FoE_i\right) \wedge \left(\cos^{-1}(\boldsymbol{n_S} \cdot \boldsymbol{p_{BiS}}) \leq FoV\right) \\ c_{2i} = \|\boldsymbol{P_S} - \boldsymbol{P_{Bi}}\| \leq R \\ c_{3i} = h_{coll,i} > D/(2 \cdot \sin\gamma) \end{cases} \tag{12}$$

A schematic representation of the detection model and its variables can be seen in Fig. 7. This illustration also shows the connections with the VisNav model, described in section 2.1. At each time step, the RLV state is fed into the detection model, which updates the sensor position and pointing vector. Then, the visibility of each of the ACCD's beacons is determined, and returned to the VisNav model – together with the position of the beacons in the ACCD body frame. The fixed parameters associated with the ACCD docking cone are given in Table 1. The parameters associated with beacons and VisNav sensor are determined using a sensitivity study presented in the next sub-section.

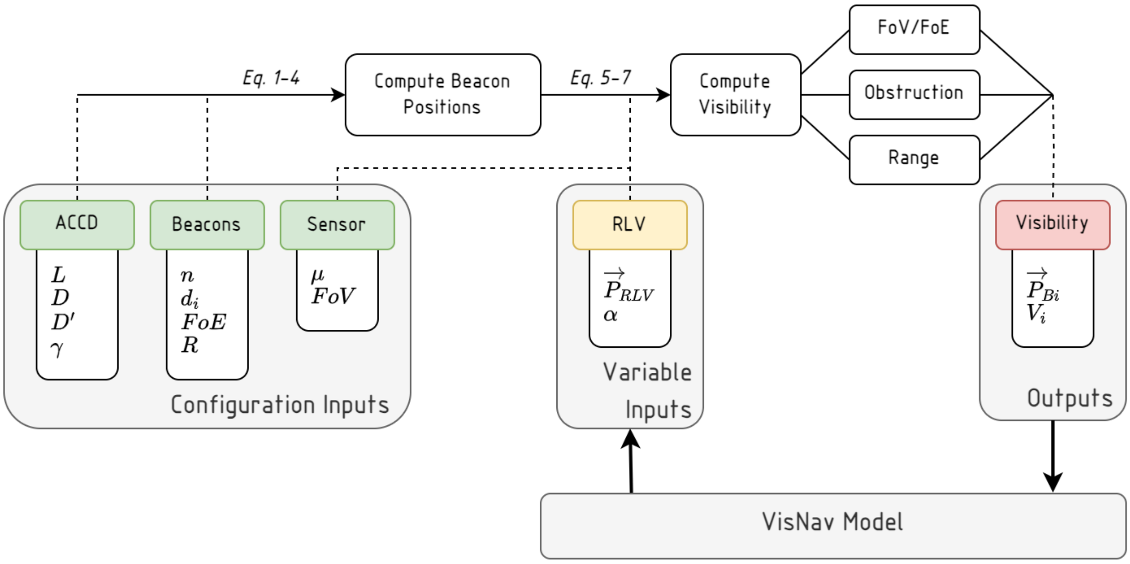

Fig. 7: Flow diagram of detection model

Table 1. Input parameters characterizing the ACCD docking cone

Parameter	Value(s)	Unit
L	2	[m]
D	0.7	[m]
D'	0.5	[m]
γ	30	[°]

2.3. Baseline Sensor and Beacon Configuration

Using the detection model, the expected performance of different beacon configurations is assessed, by varying the RLV position $\boldsymbol{P_{RLV}}$ in a grid search, and determining the number of visible beacons at each of these positions. Examples of the resulting approach maps for the RLV are shown in Fig. 8. It can be observed from the figure that a lower sensor mounting angle is favourable for steep descents while a higher mounting angle enables detection of more beacons in a shallower descent trajectory of the RLV. For the current study, the FoV of sensor is assumed to be 60° [40] and the FoE of each beacon is assumed to be 45°. Based on these specifications and the reference trajectory for the study (shown in Fig. 14), the maximum visibility was achieved at a sensor mounting angle (μ) of 140°.

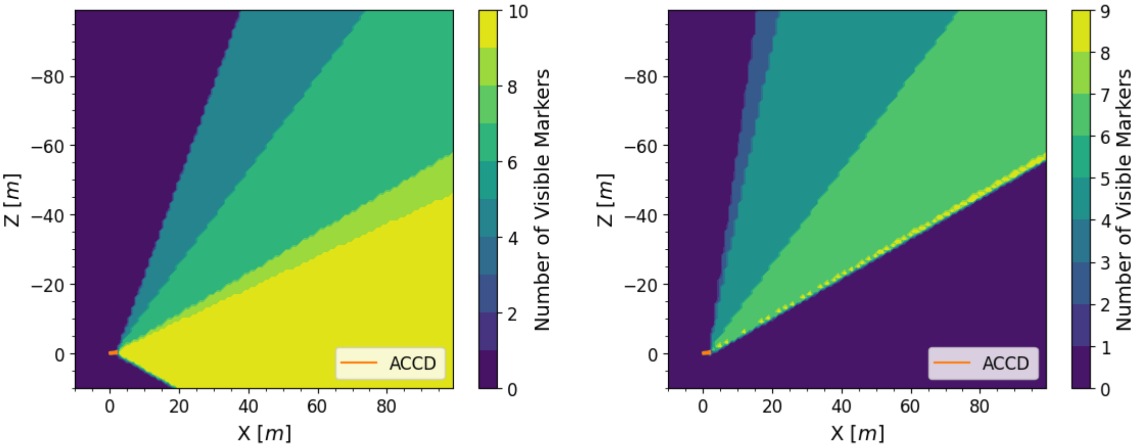

Fig. 8: Approach maps for two different VisNav configurations with different sensor mounting angles μ=160° (left) and μ=100° (right)

Table 2: Specifications of different beacon configurations on ACCD docking cone

	Beacons per Ring	**Ring Diameter (d_i)**
Configuration 1	$[6, 6]$	$1.05 * D, \quad 0.95 * D$
Configuration 2	$[6, 6]$	$1.05 * D, \quad 0.65 * D$
Configuration 3	$[3, 4, 5]$	$1.05 * D, \ 0.95 * D, \ 0.65 * D$

According to [34], the accuracy of VisNav depends on beacon geometry. Thus, the study is performed with different beacon configurations specified in Table 2 and visualized in Fig. 9. A total of 12 beacons are distributed over concentric rings on the ACCD docking cone. Each configuration has one ring of rim-mounted beacons, as indicated by Arrangement 1 in Fig. 6. The inner rings use the Arrangement 2 shown in Fig. 6. Then, using the reference trajectory shown in Fig. 14, each configuration is evaluated for visible beacons as well as accuracy of measurements. In Configuration 1, most of the beacons are placed on the outer edge of the ACCD cone. Although the placement facilitates the detection of higher number of beacons at long range at the beginning of the trajectory (shown in Fig. 10), inaccuracies arise in the final phases of docking. This can be observed in Fig. 11, which shows the relative attitude measurements from the VisNav sensor. Errors up to 1.5° can be observed in pitch and yaw configurations.

This issue is resolved by placing the inner ring slightly away from the outer ring (Configuration 2) or adding an additional ring of beacons (Configuration 3). It can be observed from Fig. 11, that the relative attitude errors decrease significantly compared to Configuration 1 and therefore, are more suitable for precision mating operations in In-Air Capturing. However, more beacons are detected in Configuration 3 compared to Configuration 2 at close-range towards the end of the trajectory (see Fig. 10). Hence, Configuration 3 is preferable to achieve higher beacon visibility during the final phases of docking. Additionally, the asymmetric arrangement of beacons in this configuration provides robustness for orientation measurements. Since the performance of both the configurations (2 and 3) are similar, Configuration 3 is selected as the baseline for the current study. The final positions of the beacons with respect to the ACCD body fixed frame are given in Table 3.

Table 3. Position of beacons in ACCD body frame, for the chosen baseline configuration – Configuration 3

Beacon	**1**	**2**	**3**	**4**	**5**	**6**	**7**	**8**	**9**	**10**	**11**	**12**
X [m]	1.79	1.79	1.79	1.97	1.97	1.97	1.97	2.00	2.00	2.00	2.00	2.00
Y [m]	0.23	-0.11	-0.11	0.33	0.00	-0.33	0.00	0.37	0.11	-0.30	-0.30	0.11
Z [m]	0.00	0.20	-0.20	0.00	0.33	0.00	-0.33	0.00	0.35	0.22	-0.22	-0.35

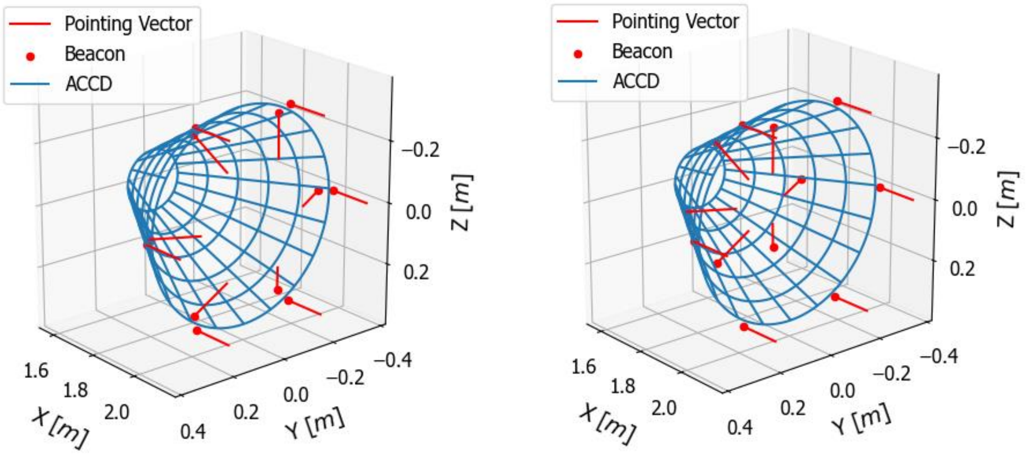

a) Configuration 1

b) Configuration 2

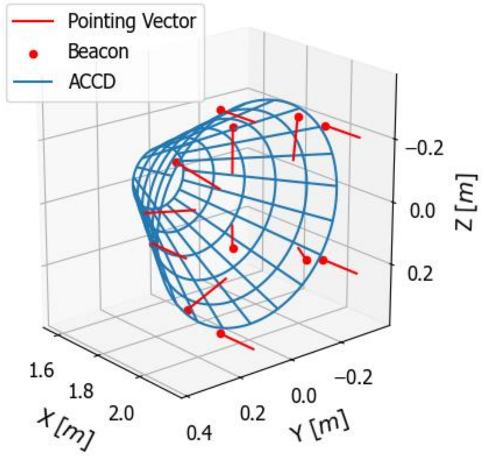

c) Configuration 3

Fig. 9: 3D visualization of different beacon configurations mounted on the ACCD's docking cone

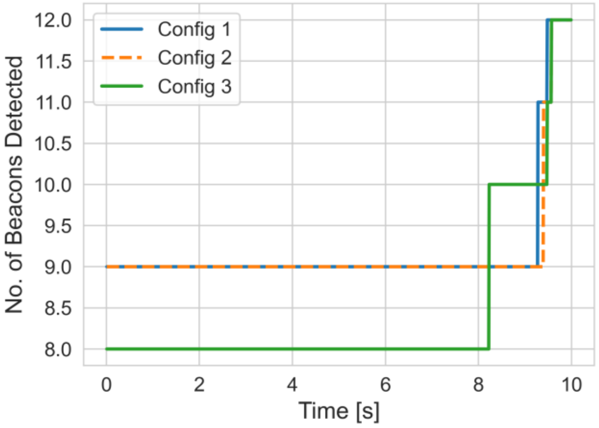

Fig. 10: Number of beacons visible throughout the trajectory of RLV given in section 4

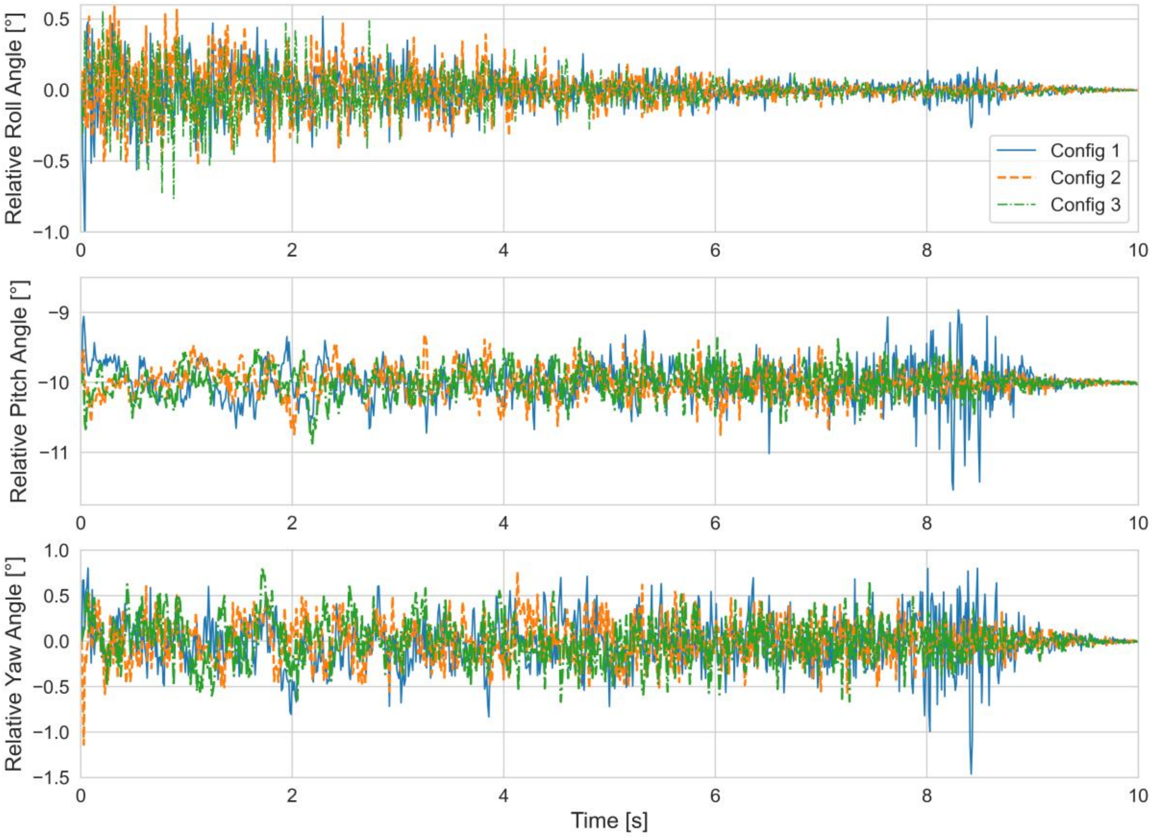

Fig. 11: Relative attitude between ACCD and RLV measured with VisNav, based on the reference trajectory given in section 4

3. Relative Navigation Model

For successful mating, the navigation system should measure the relative position with an accuracy of up to 0.35 m (slightly less than the outer radius of the ACCD guiding cone) and a relative orientation of 1°. This requirement can be met using the available sensors on the vehicles used for 'In-Air Capturing'. Fig. 12 shows the distribution of sensors available for relative navigation between ACCD and RLV. The active VisNav beacons are arranged on the ACCD docking cone while the VisNav camera is mounted on the RLV as discussed in the previous section. A set of GPS and INS sensor systems is included on both vehicles. It is assumed that a wireless communication system facilitates the sharing of GPS and IMU measurements between the two vehicles, ensuring that both sets of measurements are accessible for processing without delay. The data is fused together at their respective update rates using a simple master Extended Kalman Filter (EKF) assumed to be present on the RLV.

In the current study, three main architectures are studied for 6DOF close-range navigation (up to 200 m). The assessment involves comparing the standalone VisNav sensor, the traditional GPS/INS system, and a more comprehensive architecture combining all three systems, and evaluating their individual performances. In the coming section, specifications of the individual systems used in the simulations are explained.

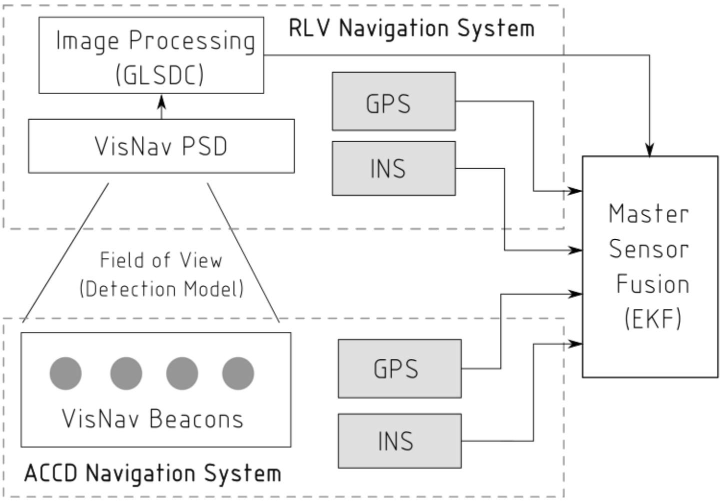

Fig. 12: Distribution of sensors and sensor fusion architecture for In-Air Capturing

3.1. VisNav Only

The VisNav system is capable of providing 6DOF measurements with an error of 1% in range and 0.1° in azimuth/elevation up to a range of 30 m and 1° error in direction for ranges up to 200m at 100Hz update rates [24],[40]. To model the measurement errors, a gaussian noise with zero mean and a standard deviation of 3500 µrad is considered [43]. The measurements obtained from VisNav (after data processing with GLSDC) could potentially be inputted into an EKF to enhance the navigation solution, giving supplementary estimations of relative velocity and acceleration. Further, it also provides the system with a prediction model using the simplified dynamics of the reference trajectory stated in Section 4. Details of EKF formulation can be found in [41]. The simplified linear dynamics used in the EKF is given by:

$$\dot{\boldsymbol{x}}(t) = \begin{bmatrix} \dot{\boldsymbol{z}}(t) \\ \ddot{\boldsymbol{z}}(t) \\ \dddot{\boldsymbol{z}}(t) \end{bmatrix} = \begin{bmatrix} 0 & I & 0 \\ 0 & 0 & I \\ 0 & 0 & 0 \end{bmatrix} \begin{bmatrix} \boldsymbol{z}(t) \\ \dot{\boldsymbol{z}}(t) \\ \ddot{\boldsymbol{z}}(t) \end{bmatrix} + \begin{bmatrix} 0 \\ 0 \\ I \end{bmatrix} \boldsymbol{w}(t) \tag{13}$$

Here,

$$\boldsymbol{z}(t) = \begin{bmatrix} \mathbf{o}(t) \\ \mathbf{p}(t) \end{bmatrix}$$

Where $\mathbf{o}$ and $\mathbf{p}$ indicate the position and orientation of the system. I is a (6×6) identity matrix and $\boldsymbol{w}$ represents the process noise in the system. It is assumed that the relative translational and rotational accelerations are zero. This is valid assumption for the current reference trajectory (shown in Fig. 14) because the RLV is assumed to be descending with a constant velocity relative to the ACCD position. The current model also does not consider the effect of control input $\boldsymbol{u}(t)$. Future simulations will include a more intricate dynamics model for prediction of the state using EKF.

Using the reference trajectory given in Section 4, Fig. 13 shows the residual error in position of the RLV relative to ACCD using the VisNav (GLSDC) data alone and using GLSDC combined with EKF. It can be observed that lower errors and smoother response can be obtained by incorporating EKF with the GLSDC algorithm used to process VisNav data. Henceforth, all the simulations associated with VisNav in the study will include both GLSDC and EKF algorithms.

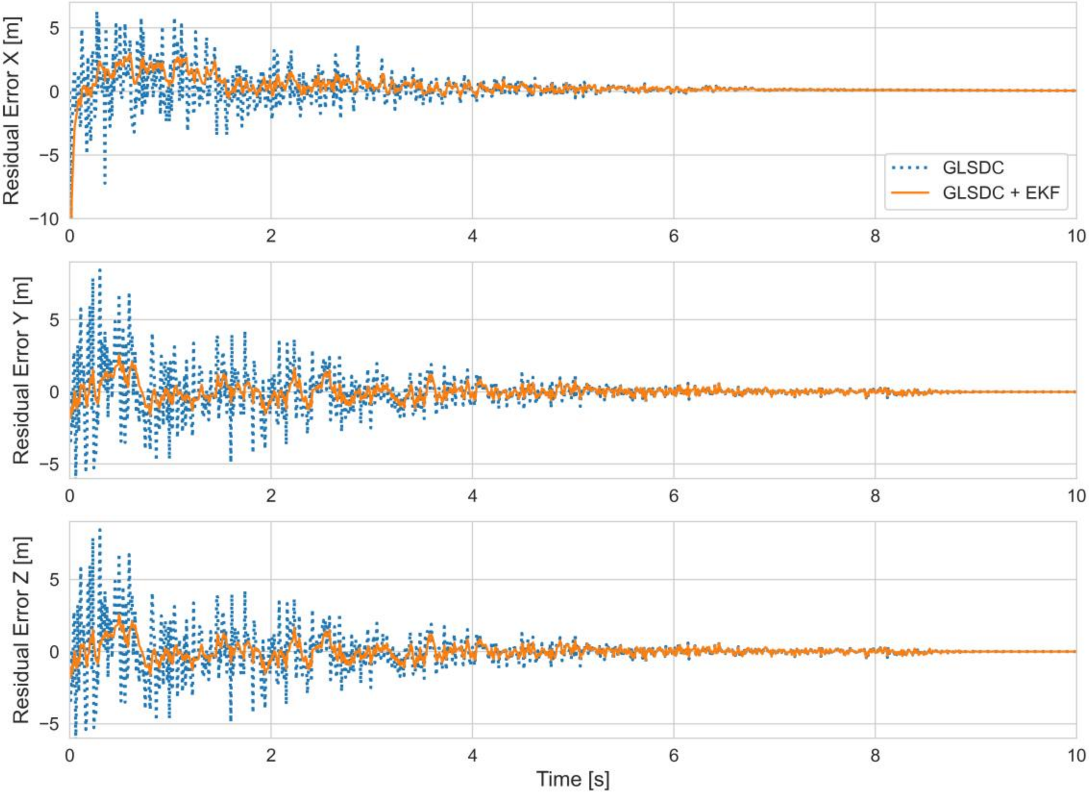

Fig. 13: Relative position error between ACCD and RLV with reference trajectory using GLSDC alone and GLSDC combined with EKF

3.2. GPS/INS

The prevalent method for relative navigation typically involves using relative GPS measurements to align with the relative INS [20]. This necessitates that each vehicle be equipped with a complete set of both GPS and INS sensors. Typically, GPS measurements can include satellite clock errors, atmospheric delays (ionospheric and tropospheric), multipath effects, and errors in the satellite's orbit data. These errors contribute to inaccuracies in the GPS position and velocity measurements. For this study, the GPS measurement error is simulated by introducing a nominal Gaussian noise with a standard deviation of 1.5 m to the position measurements [42]. A standard INS system includes accelerometers to measure linear acceleration and gyroscopes to measure angular velocity in the inertial frame. Initial position errors, integration drift (error accumulation over time due to inaccuracies in measured accelerations), and errors due to inaccuracies in the INS sensors (accelerometers and gyros) are typical errors observed in INS systems. Based on errors provided in [43], a gaussian noise with a standard deviation of 7500 μrad/s is considered in the gyroscope measurements and a standard deviation of 0.05 m/s^2 is considered for the accelerometer measurements.

The integration of GPS and INS systems helps mitigate some of these errors. The GPS provides long-term stability and helps correct the INS drift errors, while the INS offers high-rate, real-time data that can fill the gaps when GPS signals are not available or are degraded. In this study, the INS system, with a higher update rate of 100 Hz is used to predict the system state while the less frequent GPS measurements are used as updates at 10 Hz. An EKF is again used to fuse the data at different frequencies.

3.3. GPS/INS/VisNav

Although, GPS/INS system can provide good accuracy up to a tenth of a meter for relative navigation, they are subjected to a number of conditions. GPS data may not be reliable in all regions of the world and the accuracy may vary from one location to another. Moreover, multiple vehicles in the vicinity can cause GPS signals to be distorted by the aircraft. The lower update rates can also prove to be disadvantageous in case the ACCD needs to perform quick corrective maneuvers in the final phases of docking. Hence, the GPS/INS system alone may be insufficient for effective navigation during the capture.

On the other hand, VisNav systems can suffer from beacon dropout during which sufficient beacons are not available for navigation. Additionally, beacon visibility is subjected to environmental conditions. Some beacons may not appear bright enough to be detected by the VisNav sensor at longer range of operation. Thus, a combined GPS/INS/VisNav architecture can provide a robustness against beacon drop out and low visibility. Additionally, VisNav's high update rates and high accuracy at less than 30 m, provides the precision required for mating of the ACCD and RLV. In this navigation system, the INS is used for prediction/ propagation of state, the GPS is used for low frequency updates of position, and the VisNav is used for high frequency updates.

4. Simulation Results

The navigation system proposed in the previous section is tested with a simplified capture trajectory shown in Fig. 14. It is assumed that RLV starts with an initial position which is 150 m behind (X-position) and 100 m above (Z-position) the ACCD. The ACCD position is assumed to be fixed to the origin and RLV is assumed to be descending with a constant velocity relative to the ACCD. This scenario is a reduced representation of the formation flight trajectory, during which the RLV descends at a constant rate relative to the TA [2]. With the aim of achieving an accuracy of up to 0.35 m in the relative position and 1° in relative orientation between ACCD and RLV, two scenarios are evaluated.

In the first case, the RLV descends with a constant pitch angle relative to the ACCD. No disturbances are considered and the trajectory is ideal. In the second case, small disturbances in RLV pitch angle are induced to imitate exposure to turbulence. This influences the pointing direction of the VisNav sensor mounted on the RLV and simulates a non-ideal scenario where sufficient beacons are not detected by the sensor. Fig. 15 shows the beacon visibility of the two simulated scenarios. It can be observed that in the ideal scenario, a minimum of 4 beacons required for VisNav data fusion, are visible throughout the trajectory. In the non-ideal scenario, multiple beacon drop-outs are observed between 5.5 s to 8 s. In the coming sub-sections, the performance of the three navigation systems – VisNav, GPS/INS and GPS/INS/VisNav will be evaluated.

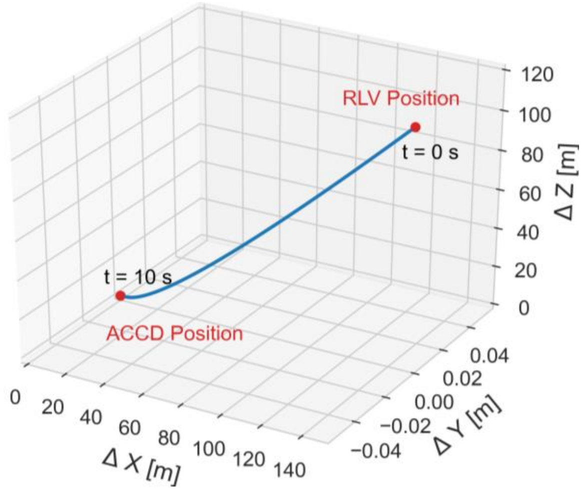

Fig. 14: Reference trajectory for approach of RLV towards ACCD during In-Air Capturing

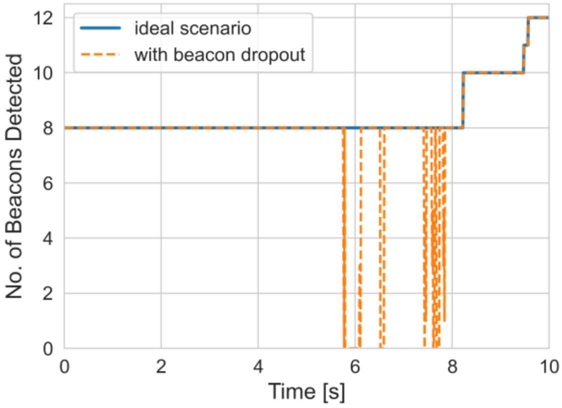

Fig. 15: Beacon visibility throughout the trajectory in ideal and non-ideal (with beacon drop out) scenarios

4.1. Ideal Scenario

Fig. 16 shows the error in relative position between RLV and ACCD using the three chosen relative navigation systems in the ideal scenario. It can be observed that the VisNav system provides higher accuracy measurements as the relative distance between the RLV and ACCD decreases. Although the error at the beginning of the trajectory is large (approximately 4 m), it quickly reduces to a small value towards the end of the trajectory, providing precise position for docking. Hence, in an ideal scenario when sufficient beacons are visible, VisNav alone can provide high accuracy navigation solution. The GPS/INS system on the other hand does not give very large errors at longer ranges but continues to have small errors throughout the trajectory. Closer to the mating point, the errors do not converge to a value below 0.35 m in all directions. Hence, the GPS/ INS system may not be sufficient for the current application. Lastly, the combined GPS/INS/VisNav system appears to converge quickly without any large errors at the beginning of the trajectory. Close to the mating point, the errors are much smaller than the required 0.35 m. The navigation solution also appears smooth and remains within the covariance bounds shown in Fig. 16. Note that the covariance bounds shown in the results are associated with the GPS/INS/VisNav system.

Similar observations can also be made in Fig. 17, which shows the error in relative orientation between ACCD and RLV. The combined GPS/INS/VisNav appears to provide the most accurate solution and converges the fastest. The VisNav system also meets the required accuracy criteria as the error converges to a small value less than 1°, close to the mating point. Although the GPS/INS model also provides a solution in which the error remains within 1°, the other two systems exhibit superior close-range performance.

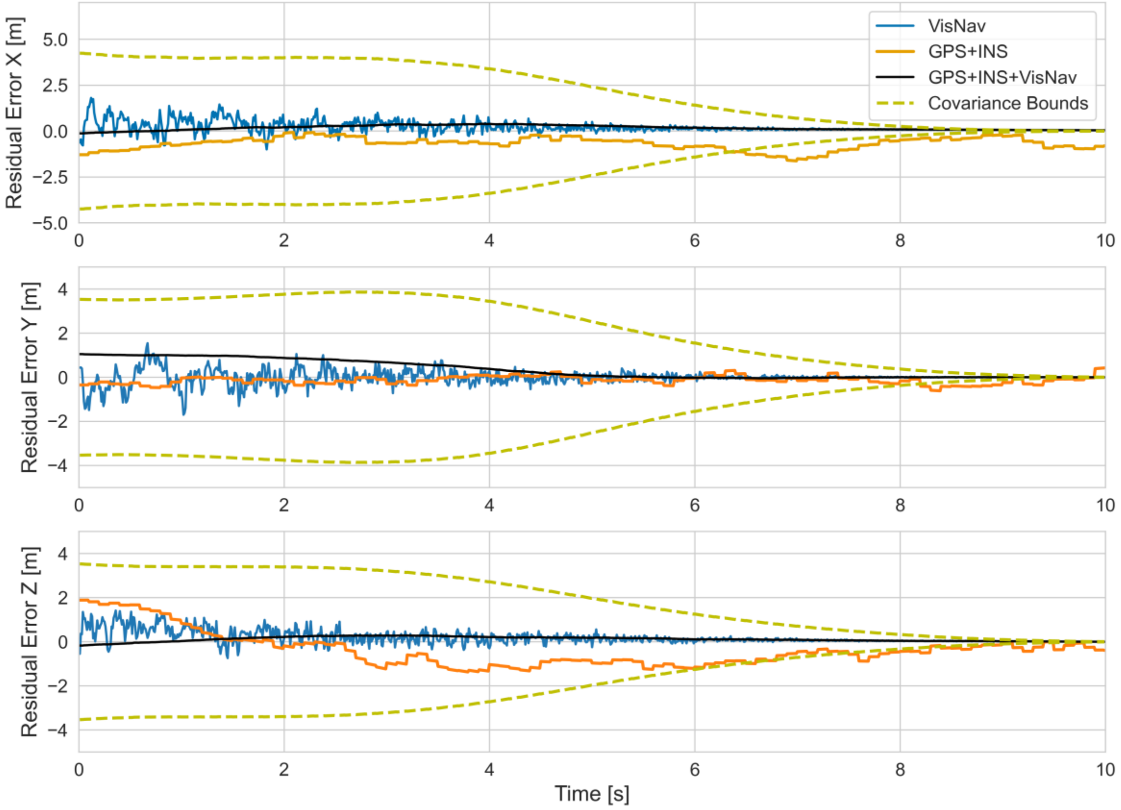

Fig. 16: Residual error in relative position between RLV and ACCD in ideal scenario

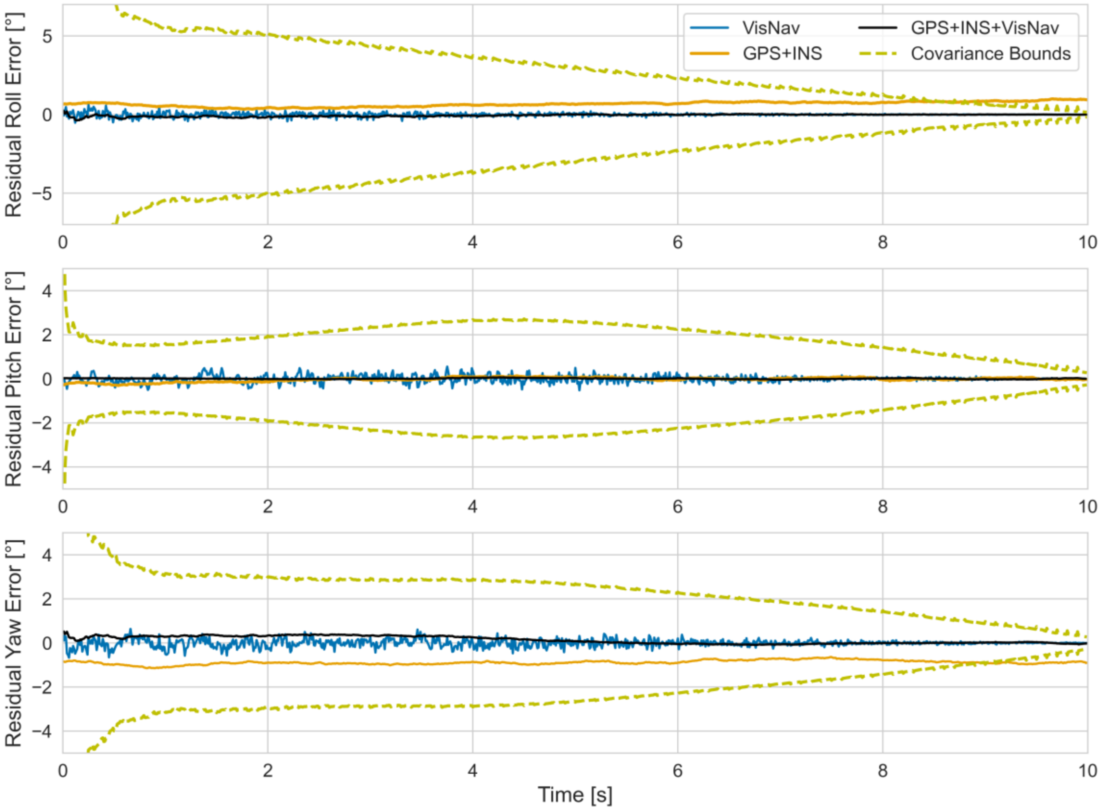

Fig. 17: Residual error in relative orientation between RLV and ACCD in ideal scenario

4.2. With Beacon Drop-Out

Since the docking maneuver of ‘In-Air Capturing’ happens behind the towing aircraft. It is likely that the ACCD and the RLV are exposed to the wake disturbances at some point in the capture trajectory. This could lead to significant disturbances in the angle of attack of both vehicles and lead to beacon drop out. Hence a non-ideal scenario is simulated to observe the effect of turbulence. In this simulation, the beacons drop out multiple times in the trajectory as shown in Fig. 15. During a beacon dropout, the last measured value by the VisNav system is held and propagated for the navigation with ‘VisNav only’. The GPS/INS navigation system is not included in this simulation as the solution will remain unaffected by the visibility of beacons. In case of the GPS/INS/VisNav system, the low frequency GPS data are used for updates in case of beacon drop-out.

Fig. 18 and Fig. 19 show the errors in relative position and orientation using VisNav and GPS/INS/VisNav systems. It can be observed that the VisNav solution for relative position starts to diverge and contains major errors during periods of beacon dropouts. This could be attributed to the simplified propagation model, which holds the last valid measurement from VisNav and propagates the solution. Since the GPS in the GPS/INS/VisNav model continues to update the position despite loss of VisNav data, the navigation system provides a reliable high accuracy solution. Additionally, since the INS measurement data is used for propagation, the system remains robust despite uncertainties in the modelling of system dynamics.

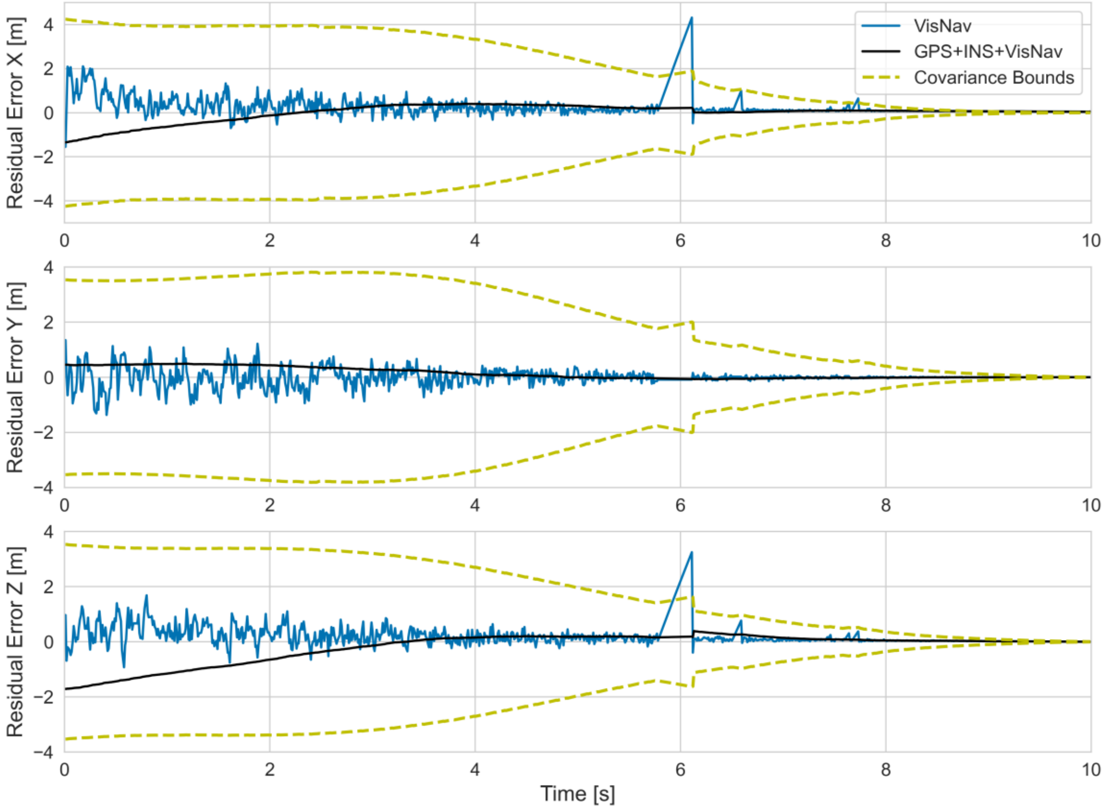

Fig. 18: Residual error in relative position between RLV and ACCD in non-ideal scenario

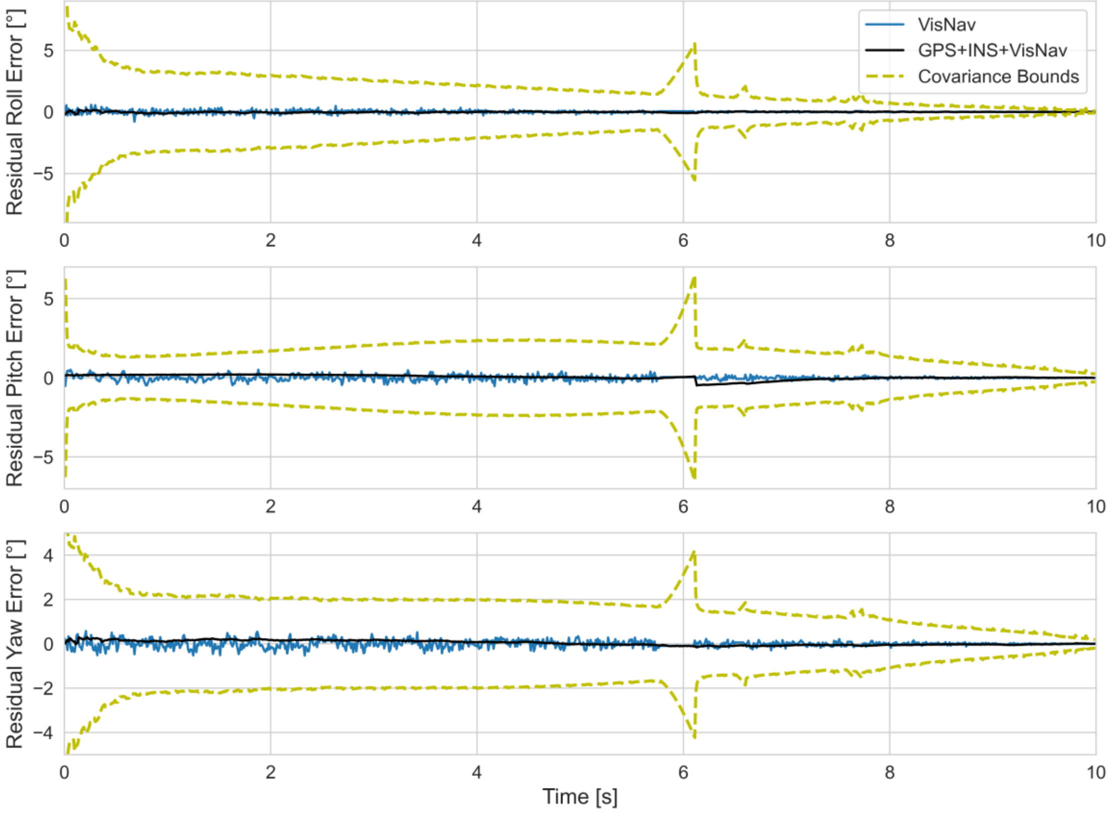

Fig. 19: Residual error in relative orientation between RLV and ACCD in non-ideal scenario

5. Conclusions and Future Work

This paper analyzes different architectures and configurations for the relative close-range navigation system for the full-scale 'In-Air Capturing' application. The 'In-Air Capturing' is a unique launcher recovery method during which, a winged Reusable Launch Vehicle (RLV) is captured mid-air by an aircraft and towed back to the launch site. An integral part of 'In-Air Capturing' is the autonomous navigation of a capturing device released from the towing aircraft to connect with the launcher stage, requiring precise close-range navigation sensors for the docking maneuver. The study examines a Vision-Based Navigation Sensor (VisNav), wherein active beacons are installed on the capturing device, and a position-sensing diode sensor is mounted on the RLV. This setup is explored as a prospective method for determining the relative position and orientation between the capturing device and RLV. Sensitivity studies are performed on placement of the beacons and orientation of sensor to improve detection and capture probability. VisNav is compared against the classical GPS/INS and a combined GPS/INS/VisNav navigation system to find the most reliable navigation system. Sensor fusion is achieved via Extended Kalman Filter (EKF) and a simplified capture trajectory is used to evaluate the performance of different configurations. Results demonstrate that GPS/INS/VisNav offers superior accuracy and a more resilient navigation solution, particularly in the face of model uncertainties and external disturbances.

Future extensions of this work will incorporate the complex dynamics from the capture trajectory, wherein the vibrations induced by the tether attached to the capturing device are included. Further, the model would integrate a high-fidelity model depicting the flowfield (wake) behind the towing aircraft, replacing the simplified model used in the current study. The measurement errors, biases and delays will also be added in more detail in the navigation model. Additionally, an improved model of system dynamics will be used in the EKF for more robust navigation. Finally, closed-loop simulations will be performed to analyze the feasibility and performance of 'In-Air Capturing'.

References

1. Patentschrift (patent specification) DE 101 47 144 C1, Verfahren zum Bergen einer Stufe eines mehr-stufigen Raumtransportsystems, released 2003.
2. Singh, S., Stappert, S., Bussler, L., Sippel, M., Kucukosman, Y. C., Buckingham, S.: Full-scale simulation and analysis of formation flight during in-air-capturing of a winged reusable launch vehicle. Journal of Space Safety Engineering, *9*(4), 541-552 (2022). https://doi.org/10.1016/j.jsse.2022.09.005
3. Stappert, S., Wilken, J., Bussler, L., Sippel, M.: A Systematic Assessment and Comparison of Reusable First Stage Return Options, Proceedings of the International Astronautical Congress (2019).
4. Calabuig, G.J.D.: Conceptual cost estimation for recovery and refurbishment operations of reusable launch vehicles, SART TN-006/2019, DLR (2019), https://elib.dlr.de/144125/ (accessed 3 April 2024).
5. Singh, S., Mastrogiuseppe, M.: Multibody modelling of tether and capture system for dynamic simulations of In-Air Capturing. Acta Astronautica 218, 59-69 (2024). https://doi.org/10.1016/j.actaastro.2024.02.008
6. Panzieri, S., Pascucci, F., Ulivi, G.: An Outdoor Navigation System Using GPS and Inertial Platform. IEEE/ASME Transactions on Mechatronics 7(2), 134-142 (2002). https://doi.org/10.1109/TMECH.2002.1011250
7. Ray, R., Cobleigh, B., Vachon, M., St. John, C.: Flight test techniques used to evaluate performance benefits during formation flight. Proceedings of the AIAA Atmospheric Flight Mechanics Conference and Exhibit (2002). https://arc.aiaa.org/doi/pdf/10.2514/6.2002-4492
8. Mammarella, M., Campa, G., Napolitano, M.R., Fravolini, M.L., Gu, Y., Perhinschi, M.G.: Machine Vision/GPS Integration Using EKF for the UAV Aerial Refueling Problem. IEEE Transactions on Systems, Man, and Cybernetics – Part C: Applications and Reviews 38(6), 197-801 (2008). https://doi.org/10.1109/TSMCC.2008.2001693

9. Johnson, D.T., Nykl, S.L., Raquet, J.F.: Combining Stereo Vision and Inertial Navigation for Automated Aerial Refueling. Journal of Guidance, Control, and Dynamics 40(9), 2250-2259 (2017). https://doi.org/10.2514/1.G002648
10. Krause, S., Cain, S.: UAV Pre-Study for In-Air-Capturing Maneuver. Proceedings of the 2020 IEEE Aerospace Conference (2020). https://doi.org/10.1109/AERO47225.2020.9172769
11. Xu, X., Duan, H., Guo, Y., Deng, Y.: A Cascade Adaboost and CNN Algorithm for Drogue Detection in UAV Autonomous Aerial Refueling. Neurocomputing 408, 121-134 (2020). https://doi.org/10.1016/j.neucom.2019.10.115
12. Wang, X., Kong, X., Zhi, J., Chen, Y., Dong, X.: Real-Time Drogue Recognition and 3D Locating for UAV Autonomous Aerial Refueling Based on Monocular Machine Vision. Chinese Journal of Aeronautics 28(6), 1667-1675 (2015). https://doi.org/10.1016/j.cja.2015.10.006
13. Li, H., Duan, H.: Verification of Monocular and Binocular Pose Estimation Algorithms in Vision-Based UAVs Autonomous Aerial Refueling System. Science China Technological Sciences 59(11), 1730-1738 (2016). https://doi.org/10.1007/s11431-016-6097-z
14. Vendra, S.: Addressing Corner Detection Issues for Machine Vision Based UAV Aerial Refueling. West Virginia University (2006).
15. Ma, Y., Zhao, R., Liu, E., Zhang, Z., Yan, K.: A Novel Autonomous Aerial Refueling Drogue Detection and Pose Estimation Method Based on Monocular Vision. Measurement 136, 132-142 (2019). https://doi.org/10.1016/j.measurement.2018.12.060
16. Khanafseh, S.M., Pervan, B.: Autonomous Airborne Refueling of Unmanned Air Vehicles Using the Global Positioning System. Journal of Aircraft 44(5), 1670-1682 (2007). https://doi.org/10.2514/1.28195
17. Doebbler, J., Valasek, J., Monda, M.J., Schaub, H.: Boom and Receptacle Autonomous Air Refueling Using Visual Snake Optical Sensor. Proceedings of the 2006 AIAA Atmospheric Flight Mechanics Conference and Exhibit (2006). https://doi.org/10.2514/6.2006-6504
18. Spencer, J.H.: Optical Tracking for Relative Positioning in Automated Aerial Refuelling. Air Force Institute of Technology (2007).
19. Chen, C.I., Koseluk, R., Buchanan, C., Duerner, A., Jeppesen, B., Laux, H.: Autonomous Aerial Refueling Ground Test Demonstration – a Sensor-in-the-Loop, Non-Tracking Method. Sensors 15(5), 10948-10972 (2015). https://doi.org/10.3390/s150510948
20. Wang, X., Dong, X., Kong, X., Li, J., Zhang, B.: Drogue Detection for Autonomous Aerial Refueling Based on Convolutional Neural Networks. Chinese Journal of Aeronautics 30(1), 380-390 (2017). https://doi.org/10.1016/j.cja.2016.12.022
21. Krause, S., Cain, S., Funke, A., González, J., Ferrándiz, M.: Overview of Planned Flight Test Operation for a Scaled In-Air Capturing Demonstration. Proceedings of the 9th European Conference for Aeronautics and Space Sciences (2022).
22. Thomas, P.R., Bhandari, U., Bullock, S., Richardson, T.S., du Bois, J.L: Advances in Air to Air Refuelling. Progress in Aerospace Sciences 71, 14-35 (2014). https://doi.org/10.1016/j.paerosci.2014.07.001
23. Gunnam, K., Hughes, D.C., Junkins, J., Kehtornavaz, N.: A DSP Embedded Optical Navigation System. Proceedings of the 6th International Conference on Signal Processing, 1735-1739 (2002). https://doi.org/10.1109/ICOSP.2002.1180137
24. Junkins, J.L., Hughes, D.C., Wazni, K.P., Pariyapong, V.: Vision-Based Navigation for Rendezvous, Docking and Proximity Operations. Proceedings of the 4th International Conference on Dynamics and Control of Space Structures (1999).
25. Krause, S.: FALCon D8.1 Technical Report – Environment Perception Flight Test Description. Deutsches Zentrum für Luft- und Raumfahrt (2023).
26. Curro II, J.A.: Automated Aerial Refueling Position Estimation Using a Scanning LiDAR. Air Force Institute of Technology (2012).

27. Parry, J., Hubbard, S.: Review of Sensor Technology to Support Automated Air-to-Air Refueling of a probe Configures Uncrewed Aircraft. Sensors 23(2), 995 (2023). https://doi.org/10.3390/s23020995
28. Lion, L., Caon, A., Olivieri, L., Branz, F., Francesconi, A.: Kinematic Tests on a Docking Mechanism for Microsatellites. CEAS Space Journal (2023). https://doi.org/10.1007/s12567-023-00516-w
29. Panzieri, S., Pascucci, F., Ulivi, G.: An Outdoor Navigation System Using GPS and Inertial Platform. IEEE/ASME Transactions on Mechatronics 7(2), 134-142 (2002). https://doi.org/10.1109/TMECH.2002.1011250
30. Krause, S.: FALCon D8.1 Technical Report – Environment Perception Flight Test Description. Deutsches Zentrum für Luft- und Raumfahrt (2023).
31. Curro II, J.A.: Automated Aerial Refueling Position Estimation Using a Scanning LiDAR. Air Force Institute of Technology (2012).
32. Chen, C.I., Stettner, R.: Drogue Tracking Using 3D Flash LiDAR for Autonomous Aerial Refueling. Laser Radar Technology and Applications XVI (2011). https://doi.org/10.1117/12.886572
33. Kelsey, J.M., Byrne, J., Cosgrove, M., Seereeram, S., Mehra, R.K.: Vision-Based Relative Pose Estimation for Autonomous Rendezvous and Docking. Proceedings of the 2006 IEEE Aerospace Conference (2006). https://doi.org/10.1109/AERO.2006.1655916
34. Tandale, M. D., Bowers, R., Valasek, J.: Trajectory tracking controller for vision-based probe and drogue autonomous aerial refueling. Journal of guidance, control, and dynamics, 29 (4), 846-857 (2006).
35. Katake, A., Choi, H.: VisNAV 100: a robust, compact imaging sensor for enabling autonomous air-to-air refueling of aircraft and unmanned aerial vehicles. Image Processing: Machine Vision Applications III, 7538, 66-76. SPIE (2010).
36. Valasek, J., Gunnam, K., Kimmett, J., Tandale, M. D., Junkins, J. L., Hughes, D.: Vision-based sensor and navigation system for autonomous air refueling. Journal of guidance, control, and dynamics, 28(5), 979-989 (2005).
37. Singh, S., Stappert, S., Buckingham, S., Lopes, S., Kucukosman, Y. C., Simioana, M., Planquart, P.: Dynamic Modelling and control of an aerodynamically controlled capturing device for 'in-air-capturing' of a reusable launch vehicle. Proceedings of 11th International ESA Conference on Guidance, Navigation & Control Systems (2021).
38. Wie, B.: Space vehicle dynamics and control. AIAA (1998).
39. Crassidis, J. L., Junkins, J. L.: Optimal Estimation of Dynamic Systems. Boca Raton, FL: Chapman and Hall/CRC (2004).
40. Katake, A., Choi, H.: VisNAV 100: a robust, compact imaging sensor for enabling autonomous air-to-air refueling of aircraft and unmanned aerial vehicles. Image Processing: Machine Vision Applications III (Vol. 7538, pp. 66-76). SPIE (2010).
41. Chui, C. K., Chen, G.: Kalman filtering (pp. 19-26). Berlin, Germany: Springer International Publishing (2017).
42. Fravolini, M. L., Ficola, A., Campa, G., Napolitano, M. R., Seanor, B.: Modeling and control issues for autonomous aerial refueling for UAVs using a probe–drogue refueling system. Aerospace science and technology, 8(7), 611-618 (2004).
43. Wang, X., Cui, N., & Guo, J.: INS/VisNav/GPS relative navigation system for UAV. Aerospace science and Technology, 28(1), 242-248 (2013).